

Design Criteria for Micro-Optical Tandem Luminescent Solar Concentrators

David R. Needell , Ognjen Ilic, Colton R. Bukowsky , Zach Nett, Lu Xu, Junwen He, Haley Bauser , Benjamin G. Lee , John F. Geisz , Ralph G. Nuzzo, A. Paul Alivisatos, and Harry A. Atwater 

Abstract—Luminescent solar concentrators (LSCs) harness light generated by luminophores embedded in a light-trapping waveguide to concentrate onto smaller cells. LSCs can absorb both direct and diffuse sunlight, and thus can operate as flat plate receivers at a fixed tilt and with a conventional module form factor. However, current LSCs experience significant power loss through parasitic luminophore absorption and incomplete light trapping by the optical waveguide. Here, we introduce a tandem LSC device architecture that overcomes both of these limitations, consisting of a poly(lauryl methacrylate) polymer layer with embedded cadmium selenide core, cadmium sulfide shell (CdSe/CdS) quantum dot (QD) luminophores and an InGaP microcell array, which serves as high bandgap absorbers on the top of a conventional Si photovoltaic. We investigate the design space for a tandem LSC, using experimentally measured performance parameters for key components, including the InGaP microcell array, CdSe/CdS QDs, and spectrally selective waveguide filters. Using a Monte Carlo ray-tracing model, we compute the power conversion efficiency for a tandem LSC module with these components to be 29.4% under partially diffuse illumination conditions. These results indicate that a tandem LSC-on-Si architecture could significantly improve upon the efficiency of a conventional Si photovoltaic cell.

Index Terms—III–V concentrator photovoltaics (PV), luminescent devices, Monte Carlo methods, quantum dots (QDs), tandem PV.

I. INTRODUCTION

LUMINESCENT solar concentrators (LSCs) offer a method to capture diffuse sunlight and maintain a relatively low manufacturing cost [1]. A traditional LSC consists of an optical

waveguide with luminophores suspended in a polymer matrix and photovoltaics (PV) material lining the waveguide's edges [2]–[4]. Both diffuse and direct sunlight incident upon this waveguide become absorbed by the embedded luminophores.

Such absorbed photons can undergo radiative recombination, which gives rise to a sharply peaked and energy downshifted photoluminescence (PL) emission spectrum. As dictated by the photoluminescence quantum yield (PLQY) of the luminophore absorbers, photons can also undergo nonradiative recombination, becoming parasitically lost as heat. Total internal reflection typically guides the PL radiation to the waveguide's edge, where it impinges upon the PV cells [5]–[7]. The light concentration factor is, therefore, proportional to the geometric gain (GG) of the LSC, defined as the ratio of illuminated waveguide area to total PV cell area.

Despite extensive research and development, LSC module concentration factors and power conversion efficiencies (PCEs) suffer from two key loss mechanisms [8]–[10]. First, embedded luminophores require near-unity PLQY in order to achieve desired optical efficiencies [11]. To prevent excess nonradiative recombination, overlap between luminophore absorbed and emitted photon energies needs to be minimized by employing luminophore species that exhibit a Stokes shift [12]–[14]. Despite advances in PLQY of various organic dyes and fluorophores, luminophores have not been traditionally able to exhibit both a sufficiently high PLQY and large Stokes shifts, leading to a significant fraction of luminesced photons to be re-absorbed by the luminophores [10], [15]–[19]. Second, the index of refraction contrast between the optical waveguide and the surrounding medium defines a photon escape cone and the limits for waveguide light trapping [13]. The LSC, therefore, experiences significant escape cone losses for light photoluminescence at angles that lie between normal incidence and the critical angle of the waveguide.

Recent advances in cadmium selenide core, cadmium sulfide shell (CdSe/CdS) quantum dots (QDs) allow for near-unity PLQY at sufficiently large Stokes shifts and ratios—where we define the Stokes shift and ratio as the separation of absorption and PL bands and the ratio of the absorption at the CdS to CdSe band edges, respectively [14], [20]. Furthermore, as shown by previous studies, the incorporation of top and bottom spectrally selective filters presents a possible approach to enhancing the waveguide light trapping efficiency [10], [12], [15], [21]–[23]. Despite these solutions targeted to maximize the optical efficiency of an LSC, only a small portion of incident light

Manuscript received March 9, 2018; revised May 19, 2018; accepted July 22, 2018. Date of publication August 10, 2018; date of current version October 26, 2018. This work was supported by the U.S. Department of Energy, Advanced Research Projects Agency for Energy under Grant DE-AR0000627. (Corresponding author: Harry A. Atwater.)

D. R. Needell, O. Ilic, C. R. Bukowsky, H. Bauser, and H. A. Atwater are with the Department of Materials Science and Applied Physics, California Institute of Technology, Pasadena, CA 91125 USA (e-mail: dneedell@caltech.edu; ilic@caltech.edu; cb@caltech.edu; hbauser@caltech.edu; haa@caltech.edu).

Z. Nett is with the Department of Chemistry, University of California Berkeley, Berkeley, CA 94720 USA (e-mail: zachnett@gmail.com).

L. Xu, J. He, and R. G. Nuzzo are with the Department of Chemistry, University of Illinois at Urbana-Champaign, Champaign, IL 61801 USA (e-mail: luxu.uiuc@gmail.com; jhe17@illinois.edu; r-nuzzo@illinois.edu).

B. G. Lee and J. F. Geisz are with the National Renewable Energy Laboratory, Golden, CO 80401 USA (e-mail: bgclee@gmail.com; john.geisz@nrel.gov).

A. P. Alivisatos is with the Lawrence Berkeley National Laboratory, Department of Materials Science and Engineering, and Kavli Energy NanoScience Institute, University of California Berkeley, Berkeley, CA 94720 USA (e-mail: paul.alivisatos@gmail.com).

Color versions of one or more of the figures in this paper are available online at <http://ieeexplore.ieee.org>.

Digital Object Identifier 10.1109/JPHOTOV.2018.2861751

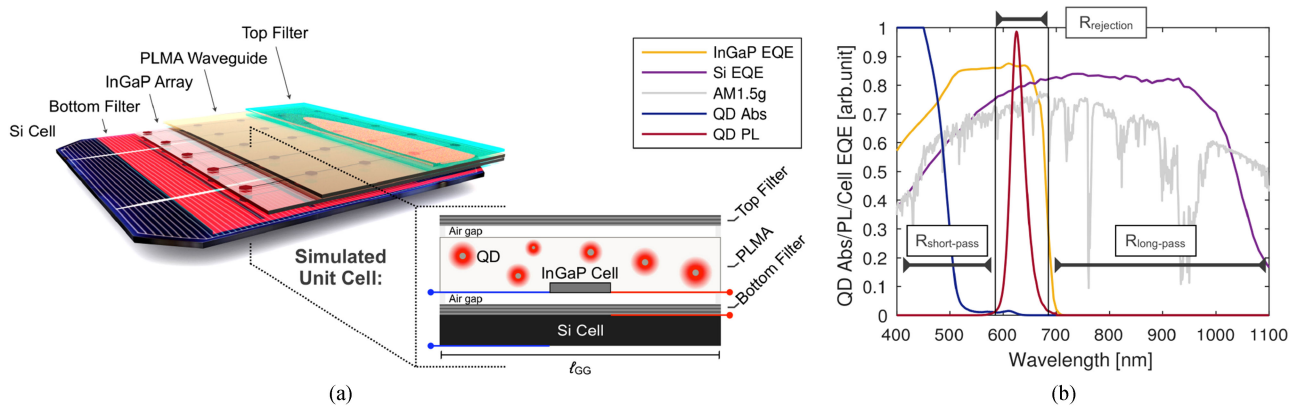


Fig. 1. (a) Three-dimensional and two-dimensional schematics of the tandem LSC-Si architecture, the QDs are enlarged for viewing purposes. (b) Measured Si and InGaP EQE curves with respect to wavelength and optimized CdSe/CdS QD absorption and PL spectra with reflectance regime definitions.

can be absorbed by the embedded luminophores. Given these limitations, LSCs are often intended for applications such as building-integrated PVs [4].

As a demonstration for another application of such LSC devices, here we optically connect a theoretical LSC component in tandem with a planar Si subcell, shown in Fig. 1(a), to function as a four-terminal tandem device. Fig. 1(b) shows the absorption and PL spectra for CdSe/CdS QDs embedded within a 30- μm -thick poly(lauryl methacrylate) (PLMA) waveguide layer [12]. This type of CdSe/CdS QD absorbs most in the short wavelength regime (400–500 nm). We spectrally match the QD PL by the use of embedded, wide bandgap InGaP microcells planar to the PLMA waveguide [24]–[27]. To complete this four-terminal tandem design, we model interdigitated back contact (IBC) Si cells for use as an example bottom cell. Fig. 1(b) displays the external quantum efficiency (EQE) of both the InGaP and Si cells.

This LSC architecture arranges the InGaP microcells in a planar geometry with respect to the optical waveguide, as shown in Fig. 1(a). With such a planar configuration, we decouple the module area from the GG and obtain an LSC form factor similar to conventional Si modules. Additionally, Bronstein *et al.* demonstrated that such a planar LSC geometry allows for increased optical efficiencies and record concentration factors [12]. We set a GG of 100 with an InGaP microcell area of 0.15 mm^2 , and therefore expose each InGaP microcell to a waveguide aperture area of 15 mm^2 .

Here, we characterize a tandem LSC-on-Si module design through the use of a Monte Carlo ray-tracing model. We model CdSe/CdS QDs whose absorption/PL data [12] spectrally match InGaP cells' known EQE [24] with simulated cell efficiency $\eta_{\text{InGaP}} = 19.3\%$ and employ an IBC Si subcell to absorb longer wavelength, nonabsorbed light with simulated cell efficiency $\eta_{\text{Si}} = 18.2\%$. Using these device components, we explore ideal spectral features of a theoretical notch-filter structure encasing the LSC waveguide. From recent work in optimized distributed Bragg reflectors and high contrast grating metasurfaces, we consider both angularly independent and dependent rejection band centers [28]–[35]. We develop optimal designs for tandem LSC-on-Si modules both with and without such notch-filter components and analyze best-case simulation scenarios.

II. RESULTS

A. LSC-on-Si Optimization Without Notch Filters

Given the large parameter space, we first perform an analysis with extensive multiparameter variations assuming no top or bottom luminescence photon-trapping filters. In our analysis, we vary the QD PL peak spectral position, the QD PL spectral full width at half maximum (FWHM), the optical density (OD) of QDs within the 30- μm -thick PLMA waveguide, and the QD PLQY. During the optimization of one parameter, we treat the rest as fixed given known characteristics of CdSe/CdS QDs. Fig. 2 shows the results of this analysis.

Without filters, the ideal PL peak location gives rise to a maximum module performance at a luminescence wavelength of slightly above 650 nm across all PLQY values, shown in Fig. 2(a), due to a Stokes shift increase, minimizing re-absorption losses at wavelengths corresponding to high InGaP cell EQE. We additionally observe an optimum FWHM for the QD PL spectrum of approximately 80 nm, as shown in Fig. 2(b). For all assumed PLQY values, we find that maximum PCE occurs at a QD OD of 0.30 at 450 nm, as shown in Fig. 2(c). For OD values less than 0.30, QDs do not absorb and re-emit enough photons to the InGaP microcells. However, for OD values greater than 0.30, photons are either parasitically absorbed by the QDs or reradiated at angles within the escape cone at a greater frequency. We find that with unity PLQY, optimized PL peak location at 650 nm, ideal FWHM, and intermediate waveguide OD, we achieve a maximum PCE of $\eta = 24.5\%$ for the no-filter waveguide design under 40% diffuse, 60% direct AM1.5 g simulations.

In the no-filter design, the majority of the output power generated by the tandem LSC-on-Si module stems from the Si subcell. From Fig. 2(d), we find the generated photocurrent of the Si cell to be an order of magnitude greater than the InGaP cell photocurrent across all PLQY. We conclude that in order to achieve both higher overall module efficiencies and more significant InGaP cell power generation, additional light-trapping mechanisms must be integrated into the device architecture.

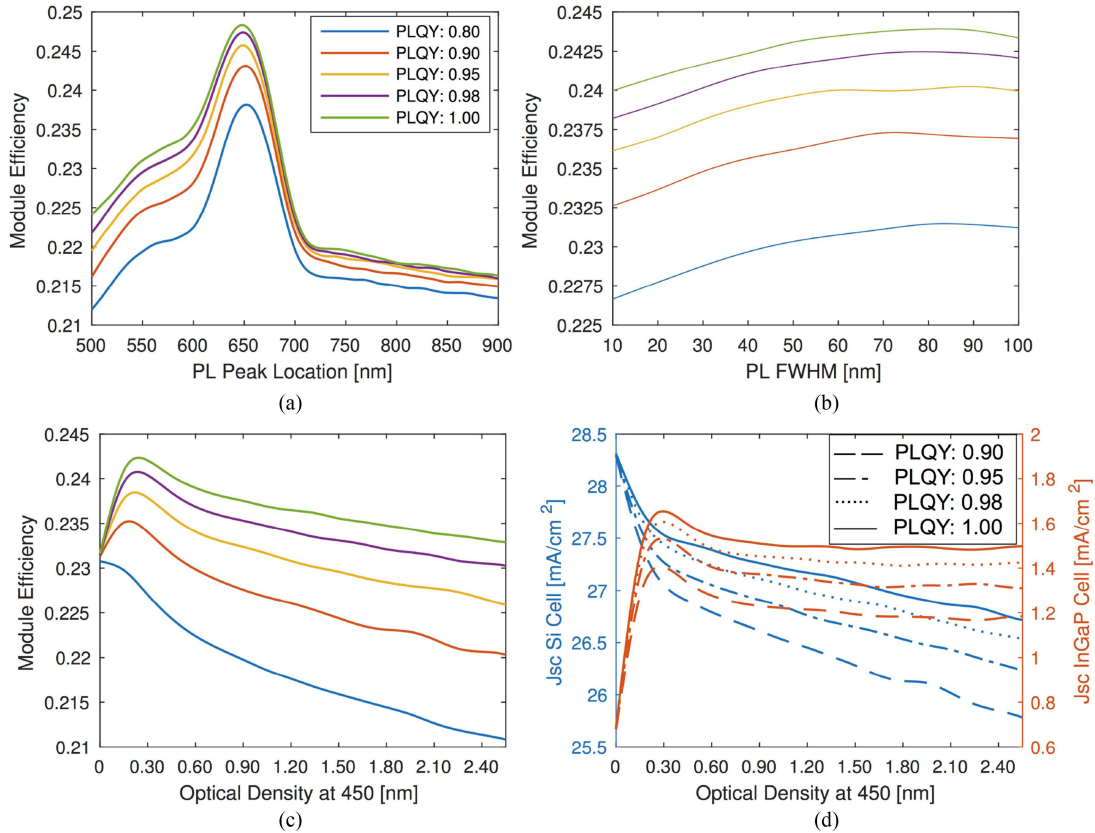


Fig. 2. Tandem LSC-on-Si module efficiency in the case without filters, with respect to varying. (a) PLQY and QD PL peak location assuming an OD of 0.30 and FWHM of 30 nm. (b) PLQY and QD PL FWHM assuming an OD of 0.30 and PL peak location of 635 nm. (c) PLQY and OD of the embedded QDs at 450 nm assuming a PL peak location of 635 nm and FWHM of 30 nm. (d) Short-circuit current of the Si and InGaP cells, varying PLQY and OD of the embedded QDs at 450 nm again assuming a PL peak location of 635 nm and FWHM of 30 nm.

B. Top and Bottom Notch-Filter Optimization

To determine optimal spectral and angular requirements for the top and bottom luminescence photon trapping notch filters, we vary the reflection parameters, with a top hat-like profile, as shown in Fig. 1(c).

Given the PL spectrum of such CdSe/CdS QDs, Fig. 3(a) shows the module PCE for various rejection-band widths. A width of 68 nm yields maximum device performance, assuming no strong angular dependence of the rejection band of the notch filter and a QD PL FWHM of 30 nm centered at 635 nm. Assuming ideal rejection-band top/bottom filter widths, we investigate the effects of filter reflectance variation, specifically $R_{\text{rejection}}$ against R_{pass} (in the short-pass and long-pass regimes). Fig. 3(c) details the overall module efficiency results, while varying the two reflection parameters $R_{\text{rejection}}$ and R_{pass} . We find that, while optimal module efficiency results from an assumed unity $R_{\text{rejection}}$ and zero R_{pass} , an increase in filter R_{pass} is more detrimental to overall device performance than a reduction in $R_{\text{rejection}}$. Assuming distinct top/bottom notch filters, we determine the overall impact on module efficiency of varying $R_{\text{short-pass}}$ for the bottom notch filter only while assuming a unity $R_{\text{rejection}}$ and zero R_{pass} for the top notch filter. Fig. 3(d) shows that the short-wavelength transmission requirements for the bottom filter can be significantly relaxed while still enabling high performance. For the optimal top and bottom angularly in-

dependent notch-filter designs obtained from this analysis, we achieve a maximum module efficiency of $\eta = 27.7\%$.

As is the case with common spectrally selective notch filters (e.g., one-dimensional photonic crystals), a greater incident photon angle often blueshifts the rejection band while maintaining a relatively constant bandwidth [31], [30], [28]. We vary the rejection band left and right edges' location for normally incident photons, and, as an example, assume a rejection band blue-shift of 1 nm per degree off-normal incidence. Fig. 3(b) shows the results of this simulation. For rejection band left and right edges located near 620 and 700 nm, respectively, we find a globally maximum module efficiency of $\eta = 25.0\%$.

C. LSC-on-Si Optimization With Notch Filters

Analogous to the optimization of the tandem LSC without spectral filters, we determine the maximum module efficiency possible with optimal top and bottom notch filters. Fig. 4(a) shows that ideal PL peak values depend strongly on the PLQY. For lower QD performance, 650 nm yields maximum module efficiency. As the limit of PLQY approaches unity, the PL peak optimum shifts to 635 nm as a result of the lossless filters allowing for unlimited photon recycling and trapping.

Similarly, we see a strong dependence of module performance on PLQY by varying the FWHM, shown in Fig. 4(b). We find that, as expected, high PLQY values favor sharply peaked

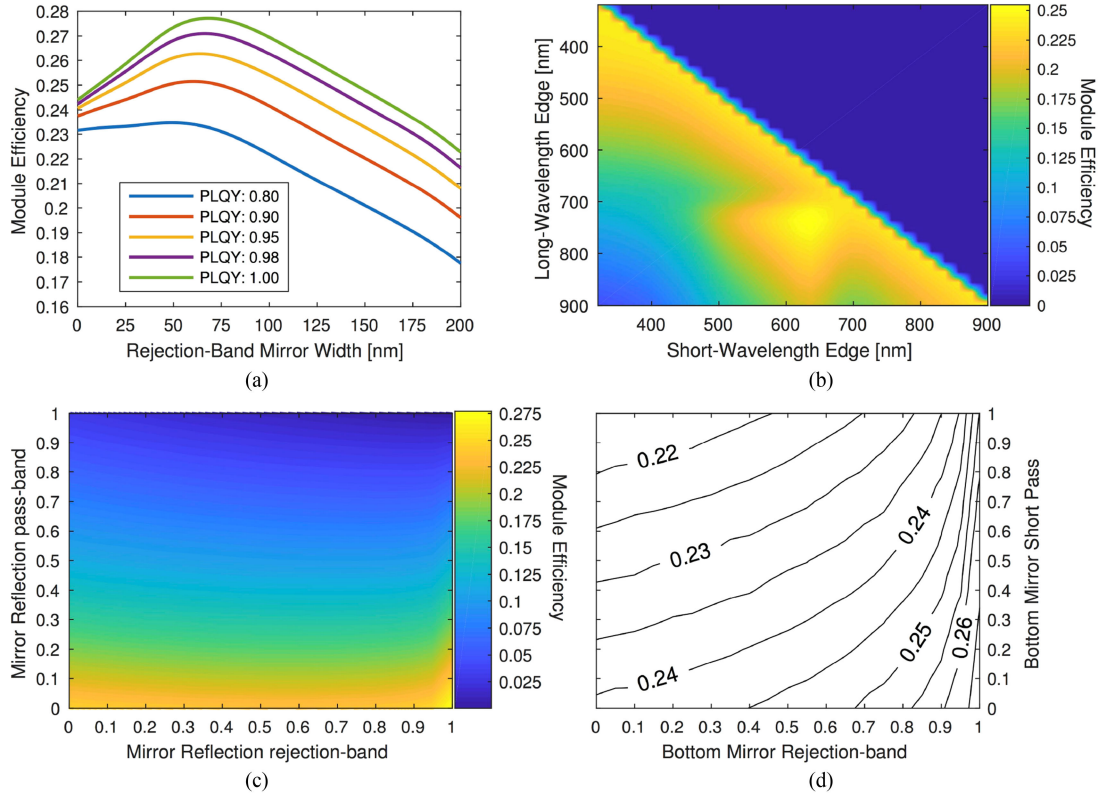


Fig. 3. Tandem LSC-on-Si module efficiency with respect to varying. (a) Rejection-band filter width, centered at 635 nm, assuming unity rejection-band reflection and unity out-band transmission. (b) Filter rejection-band left and right edges' location at DNI photons, assuming unity $R_{\text{rejection}}$ and zero R_{pass} . (c) Top and bottom filter $R_{\text{rejection}}$ vs. R_{pass} across all angles at ideal rejection-band widths. (d) Bottom-only filter $R_{\text{rejection}}$ vs. $R_{\text{short-pass}}$, assuming ideal top filter performance as shown in (c), and ideal rejection-band widths.

PL. Variation of OD of the QDs embedded within the polymer waveguide shows a strong dependence on PLQY values as well, shown in Fig. 4(c). However, in all cases, a maximum module PCE is obtained at OD of 0.30 at 450 nm. In contrast to the no-filter case, we find that the module efficiency decreases less rapidly for increasing OD with nonunity PLQY. We, therefore, find that with unity PLQY, optimized QD PL peak location, ideal FWHM, and an OD of 0.30 at 450 nm, we achieve a maximum PCE of $\eta = 29.4\%$ under 40% diffuse, 60% direct AM1.5 g simulations.

D. Optimal Case Analysis

In the perfect-filter case, the output power generated by this tandem LSC-on-Si module is much more evenly split between the Si subcell and the embedded InGaP microcells. The InGaP contributes approximately 43% of the total output power for unity PLQY, as shown in Table I. Fig. 4(d) displays the short-circuit current contribution of the InGaP cell. In contrast to Fig. 2(d), the InGaP photocurrent has increased by a factor of 4.5.

Fig. 5(b)–(d) compares the performance of the optimized no-filter and perfect-filter designs. For this, we choose a PLQY of 0.98 to determine how parasitic QD absorption loss compares to escape cone loss. We find that in the no-filter design, the largest performance detriment comes from escape cone loss, shown in Fig. 5(c). For the perfect-filter case, short-wavelength

photons are more likely to be parasitically absorbed, as a result of increased photon recycling, shown in Fig. 5(d). We demonstrate this fact by comparing the average number of PL events for a given photon of a certain wavelength, shown in Fig. 5(b). We note that even though CdSe/CdS exhibits large Stokes ratios [12], extended PL lifetimes result in more frequent re-absorption. The dominant loss mechanism for long wavelength photons in the perfect-filter design is primarily a result of the imperfect absorption of the Si subcell, matching the no-filter case. This matches well to expected loss mechanisms previously reported [36].

Table I shows the comparison between best-case scenarios of the no-filter and perfect-filter configurations, for unity and 0.98 PLQY. Additionally, Table I compares the overall power output with the use of a 25.6% cell efficiency, silicon heterojunction structure with IBCs as the subcell [37]; we also demonstrate the power output possible with this tandem LSC-Si architecture by replacing the subcell with a passivated emitter with rear contact (PERC) Si cell [38].

Finally, we investigate how the fraction of DNI light affects the overall module PCE. Fig. 5(a) shows the results of this simulation for the perfect-filter case. As expected, the highest module efficiency results from 100% DNI; however, we also note that the absolute percent efficiency increase between the completely diffuse case (i.e., 0% DNI) and the fully direct case is 0.389% absolute PCE for the LSC-on-Si module. This suggests that, while DNI light is ideal for maximum module efficiencies, this

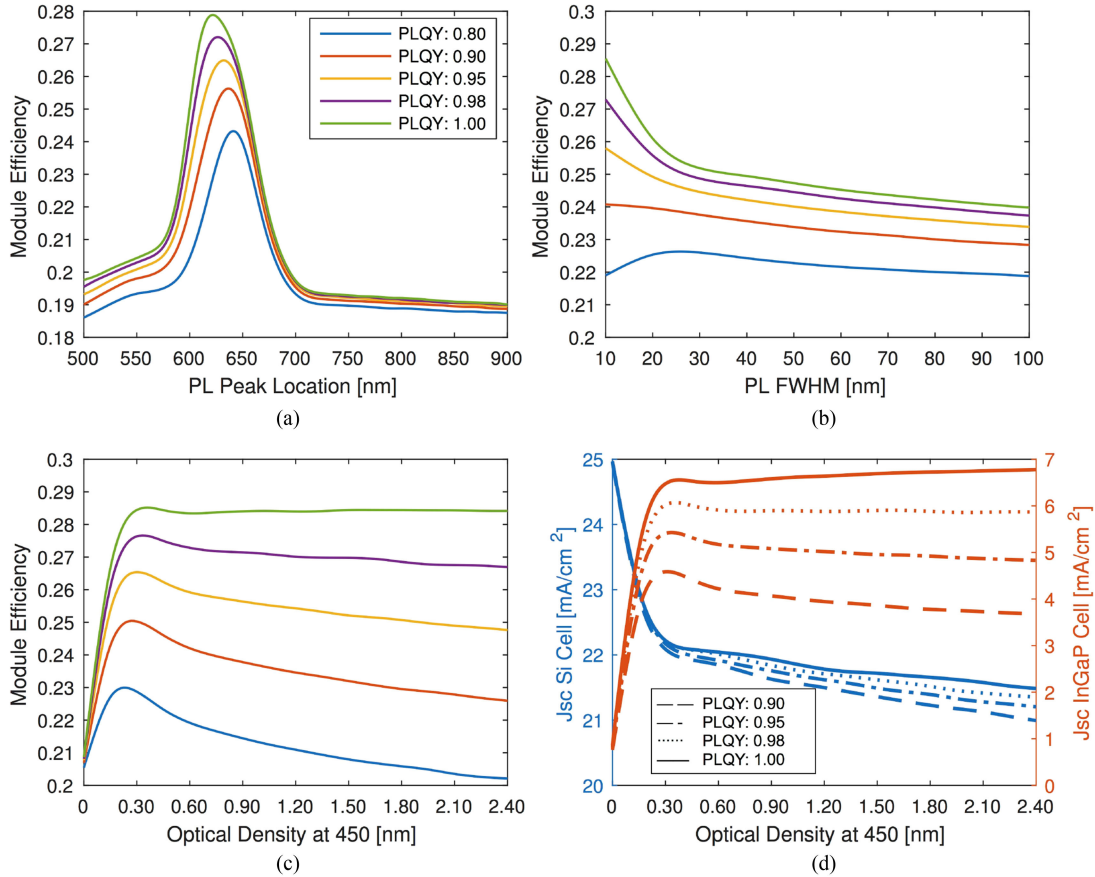


Fig. 4. Tandem LSC-Si module efficiency in the perfect-filters case with respect to varying. (a) PLQY and QD PL peak location. (b) PLQY and QD PL FWHM. (c) PLQY and OD of the embedded QDs at 450 nm. (d) Short-circuit current of the Si and InGaP cells, varying PLQY and OD of the embedded QDs at 450 nm.

tandem LSC-on-Si architecture can perform close to 30% PCE even in the completely diffuse limit. Debije *et al.* demonstrated analogous results for an LSC's performance under varying diffusivity conditions [1].

III. CONCLUSION

We have introduced a tandem-on-Si LSC design. We show significant PCE enhancements can be achieved in a tandem LSC, relative to both traditional single-layer LSC designs and flat-plate Si cells. A tandem LSC-on-Si module features a number of components that influence its conversion efficiency, including spectrally selective top and bottom filters and CdSe/CdS QD luminophores with optimally tuned absorption and PL spectra. We apply a Monte Carlo ray-tracing model to IBC Si and InGaP cells with known EQEs, which yield stand-alone, simulated cell efficiencies of $\eta_{\text{Si}} = 18.2\%$ and $\eta_{\text{InGaP}} = 19.3\%$ under direct AM1.5 conditions. We ultimately find, under 40% diffuse 60% direct AM1.5 g simulation conditions, maximum LSC-on-Si PCEs reach 24.5% and 29.4% for the no-filter and perfect-filter designs, respectively. Furthermore, if we assume Si subcell EQEs consistent with reported PERC [38] or heterojunction interdigitated back contact [37] Si cells and perfect notch filters, we find tandem LSC-on-Si PCEs of 31.2% and 32.0%, respectively.

Assuming a tandem structure without top and bottom filters, we find an ideal QD PL peak location of 650 nm given the InGaP and Si cell EQEs, optimized QD PL FWHM of 80 nm, and an OD of the embedded QDs within the PLMA waveguide of 0.30 at 450 nm. For high QD PLQY under these conditions, we find a maximum PCE of 24.5%, where roughly 10% of this power is generated by the LSC and 90% by the Si subcell.

Optimizing the top and bottom notch filters' spectral reflection and angular dependence for maximum PCE, we find for near-unity PLQY an ideal QD PL peak location of 635 nm, optimized QD PL FWHM of 10 nm, and an OD of the embedded QDs within the PLMA waveguide of 0.30 at 450 nm. Under these conditions and optimized filter design, we find a maximum PCE of 29.4%, where roughly 45% of the output power is generated by the LSC and 55% by the Si subcell.

IV. METHODS

The tandem LSC-on-Si module performance is simulated via a Monte Carlo ray-tracing model [39]–[41]. The algorithm traces photons throughout the module architecture, assuming periodic boundary conditions at the waveguide edges. We determine photon trajectories via scattering, reflection, transmission, and absorption probabilities for each component in the device. We calculate photon reflection probabilities by Fresnel laws for

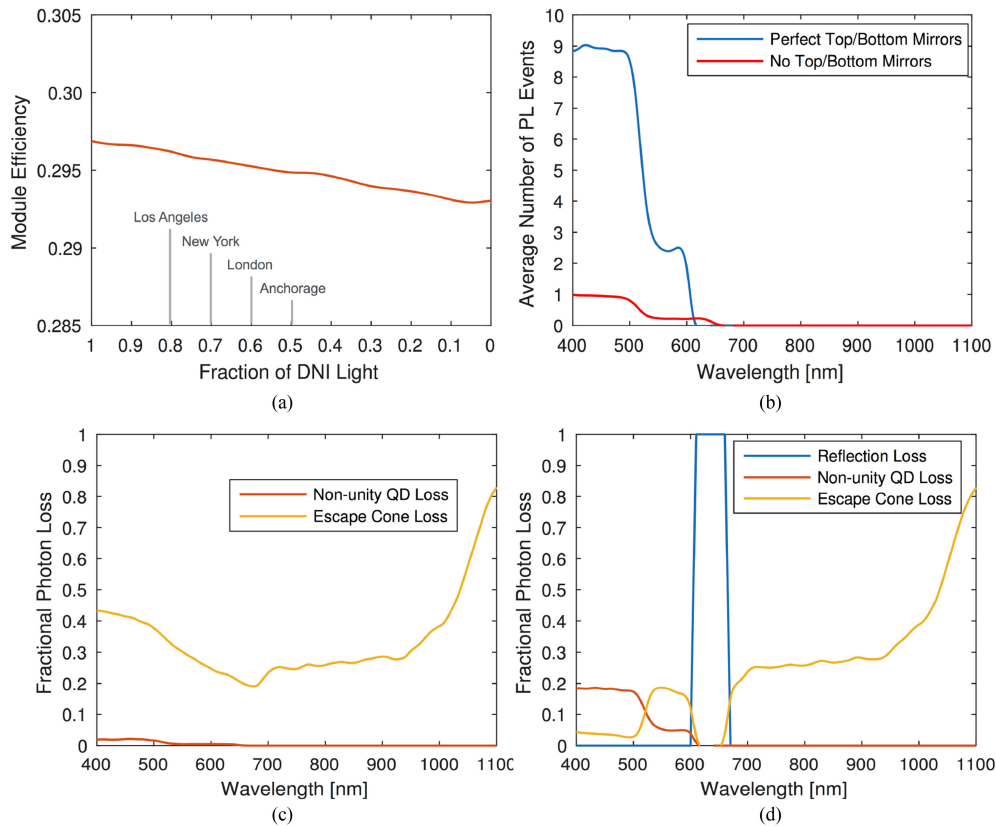


Fig. 5. (a) Comparison of the tandem LSC–Si module efficiency performance vs. the standalone Si cell efficiency, varying the fraction of light that is normally incident upon the structure. (b) Comparison between the number of QD absorption and PL events of the cases with/without filters under their respective, optimized conditions; and the tandem LSC–Si photon loss mechanisms with respect to incident photon wavelength for the (c) case without and (d) case with perfect filters under their respective, optimized conditions.

TABLE I
OPTIMAL CASE SIMULATION RESULTS

Si Cell Case	Mirror Case	PLQY	P_{out}^a (InGaP)	P_{out}^a (Si)	P_{in}^a	PCE (%)
Fabricated	None	0.98	2.18	16.61	76.77	24.4
Fabricated	None	1.00	2.18	16.65	76.77	24.5
Fabricated	Perfect	0.98	6.59	13.10	76.77	25.6
Fabricated	Perfect	1.00	9.49	13.09	76.77	29.4
PERC	Perfect	1.00	9.68	14.26	76.77	31.2
HIT	Perfect	1.00	9.60	14.95	76.77	32.0

Photoluminescence quantum yield (PLQY), power output (P_{out}), power input (P_{in}), power conversion efficiency (PCE), passivated emitted rear contact (PERC), hetero-junction interdigitated back contact (HIT).

^aMeasured in mW/cm^2 .

the TE and TM polarizations, and refraction angles via Snell's law. The algorithm assumes either complete transmission or reflection at a given interface, thereby stochastically treating photon paths [42], [43]. To achieve sufficient statistical averaging, we initialize approximately 10^6 photons for a given Monte Carlo simulation. To simulate low DNI environment, we assume 60% of incident photons to normally strike the tandem module and 40% to approach with angles uniformly distributed throughout the incident photon hemisphere—i.e., a Lambertian distribution. Cosine factor intensity losses apply to all initialized photons and determine the net incident power.

Photons impinge upon either the top filter or the LSC waveguide, for the cases with and without a notch filter, respectively. We assume a PLMA polymer waveguide (refractive index $n = 1.44$ for all wavelengths) with uniformly distributed QDs. To determine QD absorption within the polymer, we apply the Beer–Lambert law, given a certain optical loading of QDs within the PLMA [44]. We input literature CdSe/CdS QDs' absorption and PL characteristics as a baseline for Monte Carlo optimization and simulation [12]. We calculate scattering probabilities via the electric dipole approximation and insert PLMA parasitic absorption data from previous work [12].

As mentioned, the heterojunction structure of the CdSe/CdS core/shell QDs allows for fine tuning of the absorption and PL spectra. Ideally, luminophores exhibit large Stokes shifts at high PLQY in order to minimize both the number of photons parasitically absorbed by the QDs as well as the amount of light transmitted through the escape cone of the waveguide [45]. However, QD PLQY values typically decrease slightly upon dispersion in PLMA due to clumping of QDs, while PL center location remains relatively unaffected [14]. For this, we simulate PLQY varying from 0.80 to 1.00. For the Monte Carlo, we define the PLQY as the probability of photon reradiation directly after absorption by a QD.

Upon emission of the photon by the QD, we isotropically assign a radiated angle to the photon. The ray-tracing simulation assumes that the InGaP microcell is part of a larger array of cells, all planar to the waveguide as depicted in Fig. 1(a). Therefore, we assign unity reflection values to all lateral edges of the waveguide in order to simulate periodic boundary conditions.

Once a photon strikes either the embedded InGaP microcell or the Si subcell, the cell EQE determines the photon to electron conversion. We input InGaP microcells and Si subcells exhibiting EQE shown in Fig. 1(b) [24]. The EQE shown in Fig. 1(b) is an angle-averaged EQE calculated for the InGaP device when embedded in PLMA with a 70 nm ZnS antireflective coating (ARC). We calculate this EQE curve from measurements (and fitting) of larger InGaP devices in air without an ARC [24]. Because InGaP PLQY is an order of magnitude lower than QD PLQY, we do not assume any PL from the InGaP cell in this LSC system [46].

For the Si subcell, we simulate using an advanced design suitable for reaching high efficiencies, specifically an interdigitated back passivated contact (IBC) cell [47]. This back-contacted architecture frees the cell of optical shading losses. Passivated contacts enable high open-circuit voltages [48], [49]. As shown in Fig. 1(b), the IBC Si cell suffers from EQE loss in both the short wavelength regime (400–500 nm) and the longer wavelength region (700–900 nm). These loss mechanisms result from lack of a textured front surface and a suboptimal ARC.

To simulate photon reflection via front contact shading, we assign a finite probability to the InGaP cell. We do not consider shading losses resulting from interconnection of adjacent InGaP microcells. Given our Si cell EQE, this Monte Carlo simulation yields an overall PCE of $\eta_{\text{Si}} \approx 18.2\%$ and $\eta_{\text{InGaP}} = 19.3\%$ for the stand-alone Si and InGaP cells under full DNI illumination at AM1.5 g, respectively.

Photon loss mechanisms occur from either initial reflection off of the top notch filter or interface of the module, parasitic absorption via the QDs, or transmission through the top surface of the device [50]. A count of the photons and their incident wavelength accepted by either the InGaP or Si cell is integrated with respect to the standard AM1.5 g spectrum. The model then uses a detailed balance calculation of the open-circuit voltage (V_{oc}) and fill factor (FF) to give an overall tandem LSC-on-Si module efficiency [21], [51]–[53]. Note here that we define module efficiency as the generated power ratio to incident power, where the DNI:diffuse light ratio determines the incident power.

We assume an ideality factor of $n = 1$ for both the InGaP and Si cell cases and calculate the cell V_{oc} from the following equation:

$$V_{\text{oc}} = \frac{nk_B T}{q} \ln \left(\frac{I_L}{I_0} \right) + \frac{nk_B T}{q} \ln (Q_{\text{ERE}})$$

where q is the electron charge, k_B is the Boltzmann constant, T is the cell operating temperature (assumed to be $T = 300$ K), I_L is the simulated illumination current, I_0 is the dark saturation current, and Q_{ERE} is the cell's external radiative efficiency (ERE) in order to account for nonradiative effects on V_{oc} [24]. I_0 is approximated from the energy bandgaps E_g of our simulated InGaP and Si cells

$$I_0 = \frac{q}{k_B} \frac{15\sigma}{\pi^4} A_{\text{WG}} T^3 \int_{E_g/k_B T}^{\infty} \frac{x^2}{e^x - 1} dx$$

where σ is the Stefan–Boltzmann constant and A_{wg} is the waveguide area. We calculate the ERE, and therefore, the nonradiative dark-current limit, for both the InGaP and Si cells from [24], and [54] and [55], respectively. This simulation assumes a GG of 100, where we assume the InGaP microcell dimensions to be 1.5×10^{-3} m by 1×10^{-4} m, yielding an InGaP cell area of 0.15 mm^2 and, therefore, a waveguide aperture area of 15 mm^2 per unit cell.

REFERENCES

- [1] M. G. Debije and V. A. Rajkumar, "Direct versus indirect illumination of a prototype luminescent solar concentrator," *Sol. Energy*, vol. 122, pp. 334–340, 2015.
- [2] J. S. Batchelder, "The luminescent solar concentrator," Ph.D. dissertation, California Inst. Technol., Pasadena, CA, USA, 1982.
- [3] J. Madrid, M. Ropp, D. Galipeau, and S. May, "Investigation of the efficiency boost due to spectral concentration in a quantum-dot based luminescent concentrator," in *Proc. IEEE 4th World Conf. Photovolt. Energy Conf.*, 2006, pp. 154–157.
- [4] F. Meinardi *et al.*, "Highly efficient luminescent solar concentrators based on ultra-earth-abundant indirect band gap silicon quantum dots," *Nature Photon.*, vol. 11, no. 3, pp. 177–185, 2017.
- [5] A. Goetzberger and W. Greubel, "Applied physics solar energy conversion with fluorescent collectors," *Appl. Phys.*, vol. 14, pp. 123–139, 1977.
- [6] E. Yablonoitch, "Thermodynamics of the fluorescent planar concentrator," *J. Opt. Soc. Amer.*, vol. 70, no. 11, pp. 1362–1363, 1980.
- [7] E. Yablonoitch, "Statistical ray optics," *J. Opt. Soc. Amer.*, vol. 72, no. 7, pp. 899–907, 1982.
- [8] J. Gutmann, H. Zappe, and J. C. Goldschmidt, "Predicting the performance of photonic luminescent solar concentrators," in *Proc. IEEE 39th Photovolt. Spec. Conf.*, 2013, pp. 1864–1868.
- [9] W. G. J. H. M. Van Sark, Z. Krumer, C. D. M. Donegá, and R. E. I. Schropp, "Luminescent solar concentrators: The route to 10% efficiency," in *Proc. IEEE 40th Photovolt. Spec. Conf.*, 2014, pp. 2276–2279.
- [10] W. G. J. H. M. Van Sark *et al.*, "Luminescent solar concentrators – A review of recent results," *Opt. Express*, vol. 16, no. 26, pp. 21773–21792, 2008.
- [11] A. L. Martínez and D. Gómez, "Design, fabrication, and characterization of a luminescent solar concentrator with optimized optical concentration through minimization of optical losses," *J. Photon. Energy*, vol. 6, no. 4, 2016, Art. no. 45504.
- [12] N. D. Bronstein *et al.*, "Quantum dot luminescent concentrator cavity exhibiting 30-fold concentration," *ACS Photon.*, vol. 2, pp. 1576–1583, 2015.
- [13] J. C. Goldschmidt *et al.*, "Increasing the efficiency of fluorescent concentrator systems," *Sol. Energy Mater. Sol. Cells*, vol. 93, no. 2, pp. 176–182, 2009.
- [14] N. D. Bronstein *et al.*, "Luminescent solar concentration with semiconductor nanorods and transfer-printed micro-silicon solar cells," *ACS Nano*, vol. 8, no. 1, pp. 44–53, 2014.

- [15] M. G. Debije and P. P. C. Verbunt, "Thirty years of luminescent solar concentrator research: Solar energy for the built environment," *Adv. Energy Mater.*, vol. 2, no. 1, pp. 12–35, 2012.
- [16] F. Völlmer and W. Rettig, "Fluorescence loss mechanism due to large-amplitude motions in derivatives of 2,2'-bipyridyl exhibiting excited-state intramolecular proton transfer and perspectives of luminescence solar concentrators," *J. Photochem. Photobiol. A, Chem.*, vol. 95, no. 2, pp. 143–155, 1996.
- [17] J. S. Batchelder, A. H. Zewail, and T. Cole, "Luminescent solar concentrators. I: Theory of operation and techniques for performance evaluation," *Appl. Opt.*, vol. 18, no. 18, pp. 3090–3110, 1979.
- [18] B. A. Swartz, T. Cole, and A. H. Zewail, "Photon trapping and energy transfer in multiple-dye plastic matrices: An efficient solar-energy concentrator," *Opt. Lett.*, vol. 1, no. 2, pp. 73–75, 1977.
- [19] B. McKenna and R. C. Evans, "Towards efficient spectral converters through materials design for luminescent solar devices," *Adv. Mater.*, vol. 29, no. 28, pp. 1–23, 2017.
- [20] F. Meinardi *et al.*, "Large-area luminescent solar concentrators based on 'Stokes-shift-engineered' nanocrystals in a mass-polymerized PMMA matrix," *Nature Photon.*, vol. 8, no. 5, pp. 392–399, 2014.
- [21] U. Rau, U. W. Paetzold, and T. Kirchartz, "Thermodynamics of light management in photovoltaic devices," *Phys. Rev. B, Condens. Matter Mater. Phys.*, vol. 90, 2014, Art. no. 035211.
- [22] P. P. C. Verbunt *et al.*, "Increased efficiency of luminescent solar concentrators after application of organic wavelength selective mirrors," *Opt. Express*, vol. 20, no. S5, pp. A655–A668, 2012.
- [23] M. G. Debije *et al.*, "Effect on the output of a luminescent solar concentrator on application of organic wavelength-selective mirrors," *Appl. Opt.*, vol. 49, no. 4, pp. 745–751, 2010.
- [24] J. F. Geisz, M. A. Steiner, I. García, S. R. Kurtz, and D. J. Friedman, "Enhanced external radiative efficiency for 20.8% efficient single-junction GaInP solar cells," *Appl. Phys. Lett.*, vol. 103, no. 4, 2013, Art. no. 041118.
- [25] A. Reinders, M. G. Debije, and A. Rosemann, "Measured efficiency of a luminescent solar concentrator PV module called leaf roof," *IEEE J. Photovolt.*, vol. 7, no. 6, pp. 1663–1666, Nov. 2017.
- [26] M. E. Loik *et al.*, "Wavelength-selective solar photovoltaic systems: Powering greenhouses for plant growth at the food-energy-water nexus," *Earth's Future*, vol. 5, no. 10, pp. 1044–1053, 2017.
- [27] C. Corrado *et al.*, "Optimization of gain and energy conversion efficiency using front-facing photovoltaic cell luminescent solar concentrator design," *Sol. Energy Mater. Sol. Cells*, vol. 111, pp. 74–81, 2013.
- [28] D. N. Chigrin and A. V. Lavrinenko, "One-dimensional dielectric periodic structures: Total omnidirectional reflection and spontaneous emission control," *J. Lightw. Technol.*, vol. 17, no. 11, pp. 2018–2024, Nov. 1999.
- [29] D. K. G. de Boer, "Optimizing wavelength-selective filters for luminescent solar concentrators," *Sol. Energy*, vol. 7725, 2010, Art. no. 77250Q.
- [30] W. H. Southwell, "Omnidirectional mirror design with quarter-wave dielectric stacks," *Appl. Opt.*, vol. 38, no. 25, pp. 5464–5467, 1999.
- [31] H.-Y. Lee and T. Yao, "Design and evaluation of omnidirectional one-dimensional photonic crystals," *J. Appl. Phys.*, vol. 93, no. 2, pp. 819–830, 2003.
- [32] A. Arbabi, Y. Horie, M. Bagheri, and A. Faraon, "Dielectric metasurfaces for complete control of phase and polarization with subwavelength spatial resolution and high transmission," *Nature Nanotechnol.*, vol. 10, pp. 937–943, 2015.
- [33] Y. Yao, H. Liu, and W. Wu, "Spectrum splitting using multi-layer dielectric meta-surfaces for efficient solar energy harvesting," *Appl. Phys. A*, vol. 115, no. 3, pp. 713–719, 2014.
- [34] V. Karagodsky, F. G. Sedgwick, and C. J. Chang-Hasnain, "Theoretical analysis of subwavelength high contrast grating reflectors," *Opt. Express*, vol. 18, no. 16, pp. 16973–16988, 2010.
- [35] S. Darbe and H. Atwater, "Resonant dielectric high-contrast gratings as spectrum splitting optical elements for ultrahigh efficiency (>50%) photovoltaics," in *Proc. IEEE 42nd Photovolt. Spec. Conf.*, 2015, pp. 1–4.
- [36] M. G. Debije, P. P. C. Verbunt, B. C. Rowan, B. S. Richards, and T. L. Hoeks, "Measured surface loss from luminescent solar concentrator waveguides," *Appl. Opt.*, vol. 47, no. 36, pp. 6763–6768, 2008.
- [37] K. Masuko *et al.*, "Achievement of more than 25% conversion efficiency with crystalline silicon heterojunction solar cell," *IEEE J. Photovolt.*, vol. 4, no. 6, pp. 1433–1435, Nov. 2014.
- [38] M. Padmanabhan *et al.*, "Light-induced degradation and regeneration of multicrystalline silicon Al-BSF and PERC solar cells," *Phys. Status Solidi, Rapid Res. Lett.*, vol. 10, no. 12, pp. 874–881, 2016.
- [39] S. J. Gallagher, P. C. Eames, and B. Norton, "Quantum dot solar concentrator behaviour, predicted using a ray trace approach," *Int. J. Ambient Energy*, vol. 25, no. 1, pp. 47–56, 2004.
- [40] I. Papakonstantinou and C. Tummelshammer, "Fundamental limits of concentration in luminescent solar concentrators revised: The effect of reabsorption and nonunity quantum yield," *Optica*, vol. 2, no. 10, pp. 841–849, 2015.
- [41] B. S. Richards and K. R. McIntosh, "Overcoming the poor short wavelength spectral response of CdS/CdTe photovoltaic modules via luminescence down-shifting: Ray-tracing simulations," *Prog. Photovolt., Res. Appl.*, vol. 15, no. 1, pp. 27–34, 2007.
- [42] I. Coropceanu and M. G. Bawendi, "Core/shell quantum dot based luminescent solar concentrators with reduced reabsorption and enhanced efficiency," *Nano Lett.*, vol. 14, no. 7, pp. 4097–4101, 2014.
- [43] V. Sholin, J. D. Olson, and S. A. Carter, "Semiconducting polymers and quantum dots in luminescent solar concentrators for solar energy harvesting," *J. Appl. Phys.*, vol. 101, no. 12, 2007, Art. no. 123114.
- [44] Y. Zhou *et al.*, "Near infrared, highly efficient luminescent solar concentrators," *Adv. Energy Mater.*, vol. 6, no. 11, 2016, Art. no. 1501913.
- [45] J. Bomm *et al.*, "Fabrication and spectroscopic studies on highly luminescent CdSe/CdS nanorod polymer composites," *Beilstein J. Nanotechnol.*, vol. 1, no. 1, pp. 94–100, 2010.
- [46] J. F. Geisz, M. A. Steiner, I. García, S. R. Kurtz, and D. J. Friedman, "Enhanced external radiative efficiency for 20.8% efficient single-junction GaInP solar cells," *Appl. Phys. Lett.*, vol. 103, no. 4, 2013, Art. no. 041118.
- [47] S. Essig *et al.*, "Realization of GaInP/Si dual-junction solar cells with 29.8% 1-Sun efficiency," *IEEE J. Photovolt.*, vol. 6, no. 4, pp. 1012–1019, Jul. 2016.
- [48] F. Feldmann *et al.*, "Carrier-selective contacts for Si solar cells," *Appl. Phys. Lett.*, vol. 104, no. 18, 2014, Art. no. 181105.
- [49] U. Römer *et al.*, "Ion implantation for poly-Si passivated back-junction back-contacted solar cells," *IEEE J. Photovolt.*, vol. 5, no. 2, pp. 507–514, Mar. 2015.
- [50] B. C. Rowan, L. R. Wilson, and B. S. Richards, "Advanced material concepts for luminescent solar concentrators," *IEEE J. Sel. Topics Quantum Electron.*, vol. 14, no. 5, pp. 1312–1322, Sep./Oct. 2008.
- [51] P. Baruch, A. De Vos, P. T. Landsberg, and J. E. Parrott, "On some thermodynamic aspects of photovoltaic solar energy conversion," *Sol. Energy Mater. Sol. Cells*, vol. 36, no. 2, pp. 201–222, 1995.
- [52] M. Y. Levy and C. Honsberg, "Rapid and precise calculations of energy and particle flux for detailed-balance photovoltaic applications," *Solid State Electron.*, vol. 50, nos. 7–8, pp. 1400–1405, 2006.
- [53] W. Shockley and H. J. Queisser, "Detailed balance limit of efficiency of p-n junction solar cells," *J. Appl. Phys.*, vol. 32, no. 3, pp. 510–519, 1961.
- [54] M. A. Green, "Radiative efficiency of state-of-the-art photovoltaic cells," *Prog. Photovolt., Res. Appl.*, vol. 20, pp. 472–476, 2012.
- [55] K.-H. Lee *et al.*, "Assessing material qualities and efficiency limits of III-V on silicon solar cells using external radiative efficiency," *Prog. Photovolt., Res. Appl.*, vol. 24, pp. 1310–1318, 2016.

Authors' photographs and biographies not available at the time of publication.